Supporting Information

Pd-CNT-SiO_2 nanoskein: composite structure design for formic acid dehydrogenation

Ana Sousa-Castillo,[a,b] Feng Li,[a] Enrique Carbó-Argibay,[c] Miguel A. Correa-Duarte,[b] and Anna Klinkova*[a]

[a] Department of Chemistry and Waterloo Institute for Nanotechnology, University of Waterloo, Waterloo, ON N2L 3G1, Canada
[b] Department of Physical Chemistry, Singular Center for Biomedical Research (CINBIO), Southern Galicia Institute of Health Research (IISGS), and Biomedical Research Networking Center for Mental Health (CIBERSAM), Universidade de Vigo, 36310 Vigo, Spain
[c] International Iberian Nanotechnology Laboratory (INL), Av. Mestre José Veiga s/n, 4715-330 Braga

Experimental Details

Materials

Cetyltrimethylammoinium bromide (CTAB, 99%), potassium dihydrogen phosphate (KH_2PO_4), sodium hydroxide (NaOH), glycerol, tetraethyl orthosilicate (TEOS, 98%), poly (diallyldimethylammonium chloride) (PDDA, MW, 20000-350000), poly-(sodium 4-styrenesulfonate) (PSS, MW=70000), polyvinylpyrrolidone (PVP, MW, 30000), L-ascorbic acid (AA), sodium tetrachloropalladate (II) (Na_2PdCl_4), sodium borohydride ($NaBH_4$), formic acid (FA), sodium formate (SF) and Pd on carbon were purchased from Sigma-Aldrich. Sodium carbonate (Na_2CO_3) was purchased from ACP Chemicals. Multiwalled carbon nanotubes (CNTs) 9.5 nm in diameter and 1.5 μm in length, 95% C purity, synthesized using Catalytic Chemical Vapor Deposition process (CCVD), were purchased from Nanocyl as a powder. Sulphuric acid (H_2SO_4, 96%) and nitric (HNO_3) were purchased from Panreac.

Synthesis of mesoporous SiO_2 nanospheres

Mesoporous SiO_2 nanospheres were synthetized following the procedure reported by He et al.[1] Briefly, A buffer solution (pH=7) from the mixtures of 0.8575 g KH_2PO_4 and 0.145 g NaOH in 100 mL. Subsequently, 15 mL of glycerol was added and the solution was mixed, stirred and heated to 95 ºC. Then, 0.4556 g CTAB was dissolved in 10 mL Milli-Q water it was added into the above mixture. When the solution became homogenous, 250 μL of TEOS was added slowly. This last action was repeated 11 times more with intervals of 30 min. The reaction mixture was allowed to stir for 2h. The nanospheres were separated by centrifugation and purified by EtOH:H_2O 1:1and EtOH (4500 rpm, 10 min). Finally, the product was obtained by calcination at 600 ºC, 4 h (1 ºC min^{-1}). Size distribution analysis showed a diameter of 504 ± 36 nm.

Polymer surface functionalization of SiO_2

Surface functionalization of MSN beads was achieved with Poly (diallyldimethylammonium chloride). To this end, PDDA was dissolved in 0.5 M NaCl (pH 5.0) with a final polymer concentration of 2 mg mL^{-1}. Then, 25 mL of the positively charged solution was added to the silica nanoparticles (25 mg) and stirred at room

temperature for 30 min. The excess of reagents was removed by three centrifugation−redispersion cycles with water (6000 rpm, 10 min). PSS (2 mg mL^{-1}) containing in 0.5 M NaCl was then deposited onto the coated silica particles in a similar fashion and using the same conditions, the deposition of an additional layer of PDDA.

Deposition of CNT onto SiO_2

CNTs were pre-treated with acetone and ethanol to remove organic materials, frozen with N_2 and lyophilized. Then the CNTs were oxidized by the following procedure:[2] 100 mg of MWCNTs were sonicated in 100 mL of a mixture of H_2SO_4/HNO_3(3:1) for 15 min with an ultrasonic probe (30 W) and 4 h in an ultrasonic bath. The sample was washed with a NaOH aqueous solution by three centrifugation/redispersion cycles (9000 rpm, 4 h). When the pH was stabilized at 10, the sample was sonicated with the tip sonicator for 2 h. Then, the CNTs were washed with water by three centrifugation/redispersion cycles (9000 rpm, 12 h). Finally, a stable dispersion (1.6 mg mL^{-1}) of oxidized MWCNTs (ox-CNTs) holding a negative surface charge was obtained ($\zeta = {}^{-}37.75$mV). The polymer-functionalized SiO_2 (25 mg) were coated with CNTs (700µL). Excess CNTs was removed by centrifugation. Briefly, CNT-SiO_2 were dispersed in a 25mL aqueous solution PDDA (0.5 M NaCl) upto a concentration of 2 mg mL^{-1}. Excess of PDDA was removed using three 10 min centrifugation cycles at 6000 rpm, and CNT-SiO_2 were subsequently redispersed in aqueous solution.

Synthesis and deposition of Palladium Nanoparticles onto CNT-SiO_2

Ligand-free Pd NPs were synthesized as follows: to a solution containing 0.5 mg mL^{-1} of MSN-CNT, 1.95 mL of 10 mM Na_2PdCl_4, and 250 µL of sodium borohydride (0.070 M) in 2 mM Na_2CO_3 were added as reducing agent. The resulting solution was stirred for 2 min. Then, the solution was centrifuged and purified (6000 rpm, 10 min). Size distribution analysis of these Pd NPs showed a diameter of 3.7 ± 0.4 nm.

PVP-stabilized Pd NPs were synthesized according to a method described in the literature with slight modifications.[3] Typically, an aqueous solution (22.5 mL) containing PVP (262.5 g) and AA (18.75 mg) was heated at 100 °C under reflux for 10 min. Subsequently, an aqueous solution (5.0 mL) containing Na_2PdCl_4 (10 mM) was added. The reaction was

allowed to continue at 100 °C for 3 h to obtain Pd NPs that were subsequently separated from the reaction mixture by centrifugation (17500 rpm, 90 h). The collected Pd NPs were washed 2 times with water to remove excess PVP. Finally, they were redispersed in water (20 mL). Size distribution analysis of these Pd nanoparticles (Pd NPs) showed a diameter of 3.8 ± 0.5 nm.

To obtain Pd-CNT-SiO_2 composites, 5 mL of Pd NPs was added to 25 mL of CNT-SiO_2 (1 mg mL^{-1}). The mixture was stirred at room temperature for 30 min. The excess of Pd NPs was removed by three centrifugation-redispersion cycles with water (4500 rpm, 40 min). Finally, the product was redispersed in water (10 mL).

Material Characterization

The chemical compositions of Pd based catalysts were analysed by inductively coupled plasma-atomic emission spectroscopy (ICP-AES) on a POLY SCAN 60 E. The particle sizes and size distributions were characterized by high resolution transmission electron microscope (HR-TEM) JEOL JEM-2010F. SEM images were obtained using a Hitachi S-5200 scanning electron microscope operating at an acceleration voltage of 30 kV. The surface composition of the catalysts was analyzed using X-ray photoelectron spectroscopy using ThermoFisher Scientific K-Alpha instrument.

Catalyst Performance Evaluation

The hydrogen production from FA-SF solution was carried out in a 5-mL flask at different temperatures (25-40-60-80 ºC) control by Eppendorf ThermoMixer C Typically, 400 µL of a catalyst dispersion in water (ca. 2.72 µg of Pd) was first placed in the flask, then 2.5 mL of solution containing FA (0.106 M) and SF (0.635M) was injected quickly. The reforming gas composition was analyzed using Multiple Gas Analyzer #5 (SRI MG#5) connected to a thermal conductivity detector (TCD). The content of CO was analyzed using flame ionization detector (FID) equipped with a methanizer. A standard gas mixture consisting of H_2, CO, CH_4, CO_2, N_2, C_4H_6 and C_2H_6 was used as a standard.

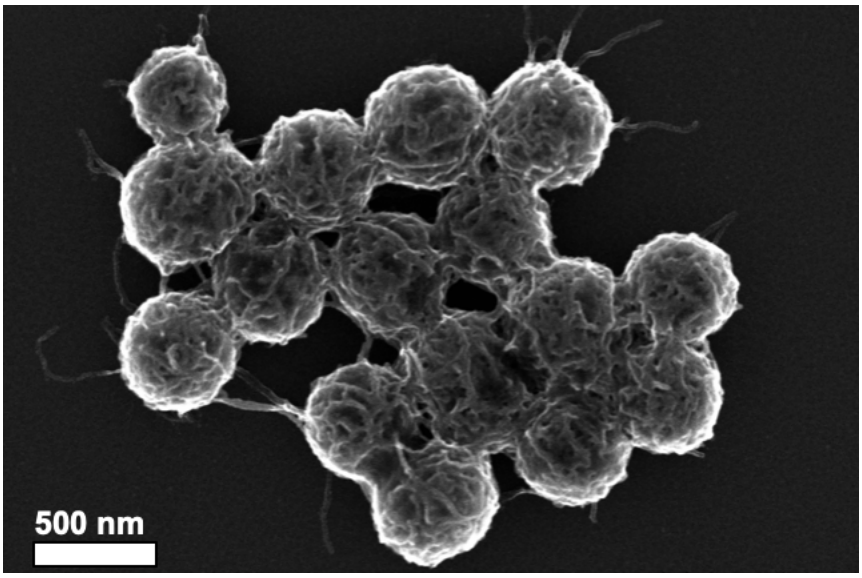

Figure S1. Low magnification SEM image of ligand-free Pd-CNT-SiO_2.

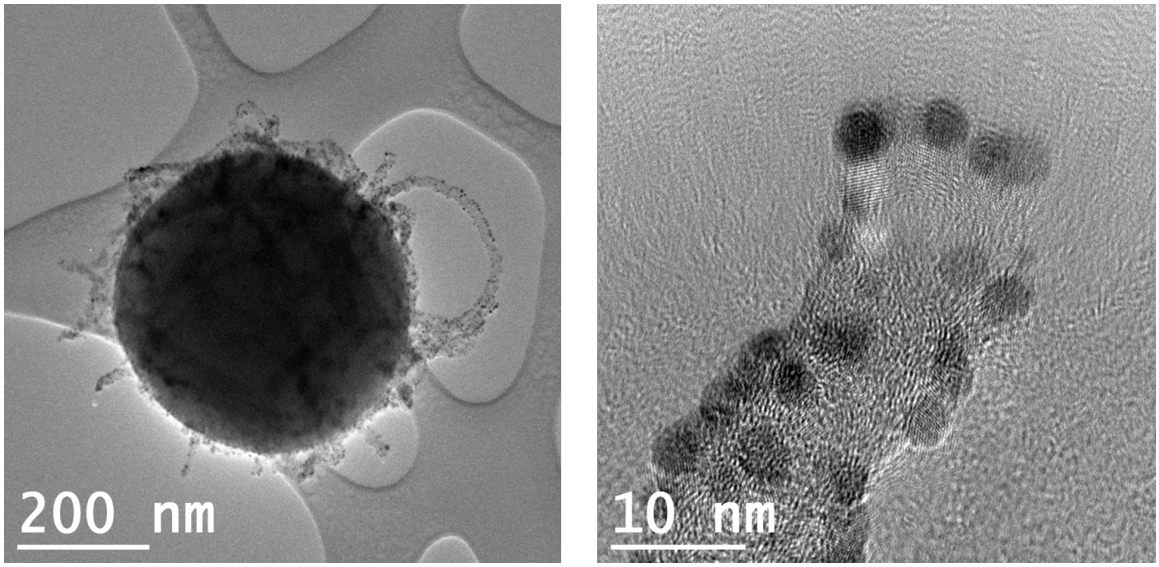

Figure S2. High resolution TEM images of ligand-free Pd-CNT-SiO_2.

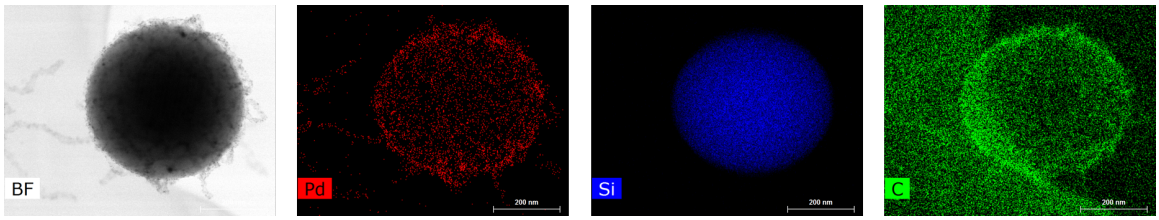

Figure S3. EDX mapping images (g) showing the distribution of Pd, Si, and C in the PVP-Pd-CNT-SiO_2 structure.

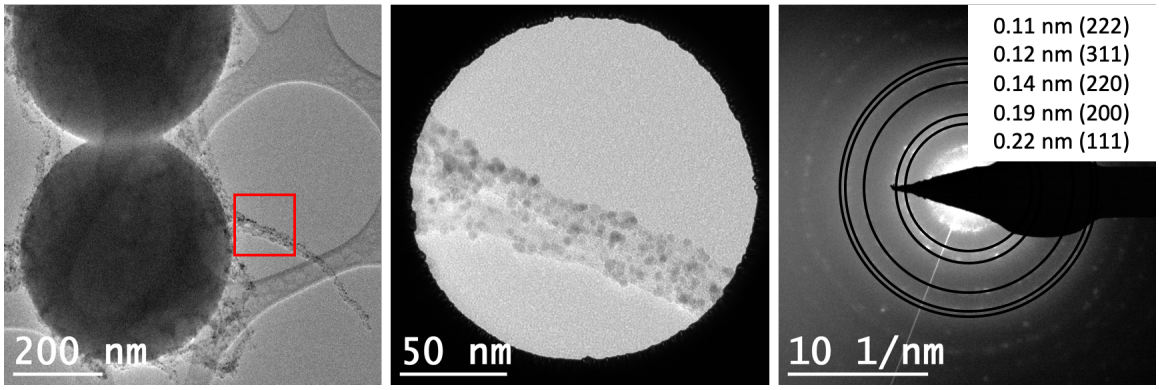

Figure S4. Selected area electron diffraction (SAED) of ligand-free Pd-CNT-SiO_2 showing a pattern for fcc Pd crystal structure (R. W. G. Wyckoff, *Crystal Structures*, 1963, 1, 7-63).

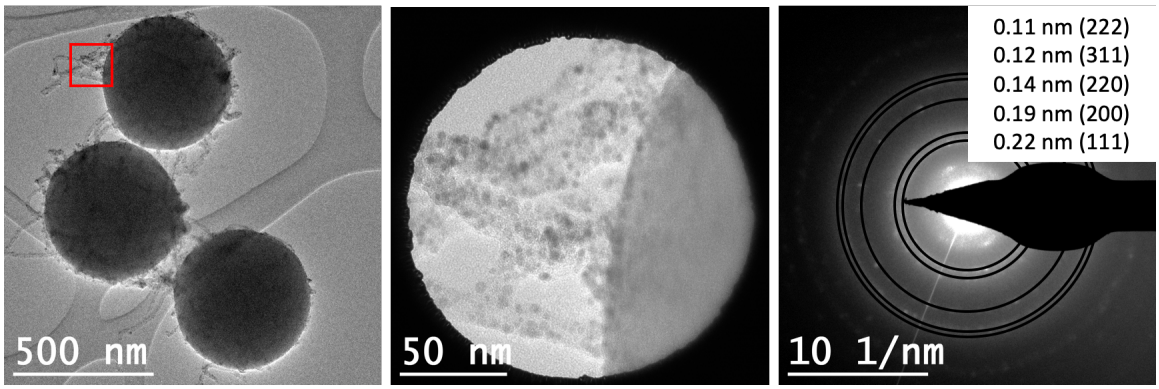

Figure S5. Selected area electron diffraction (SAED) of PVP-Pd-CNT-SiO_2 showing a pattern for fcc Pd crystal structure (R. W. G. Wyckoff, *Crystal Structures*, 1963, 1, 7-63).

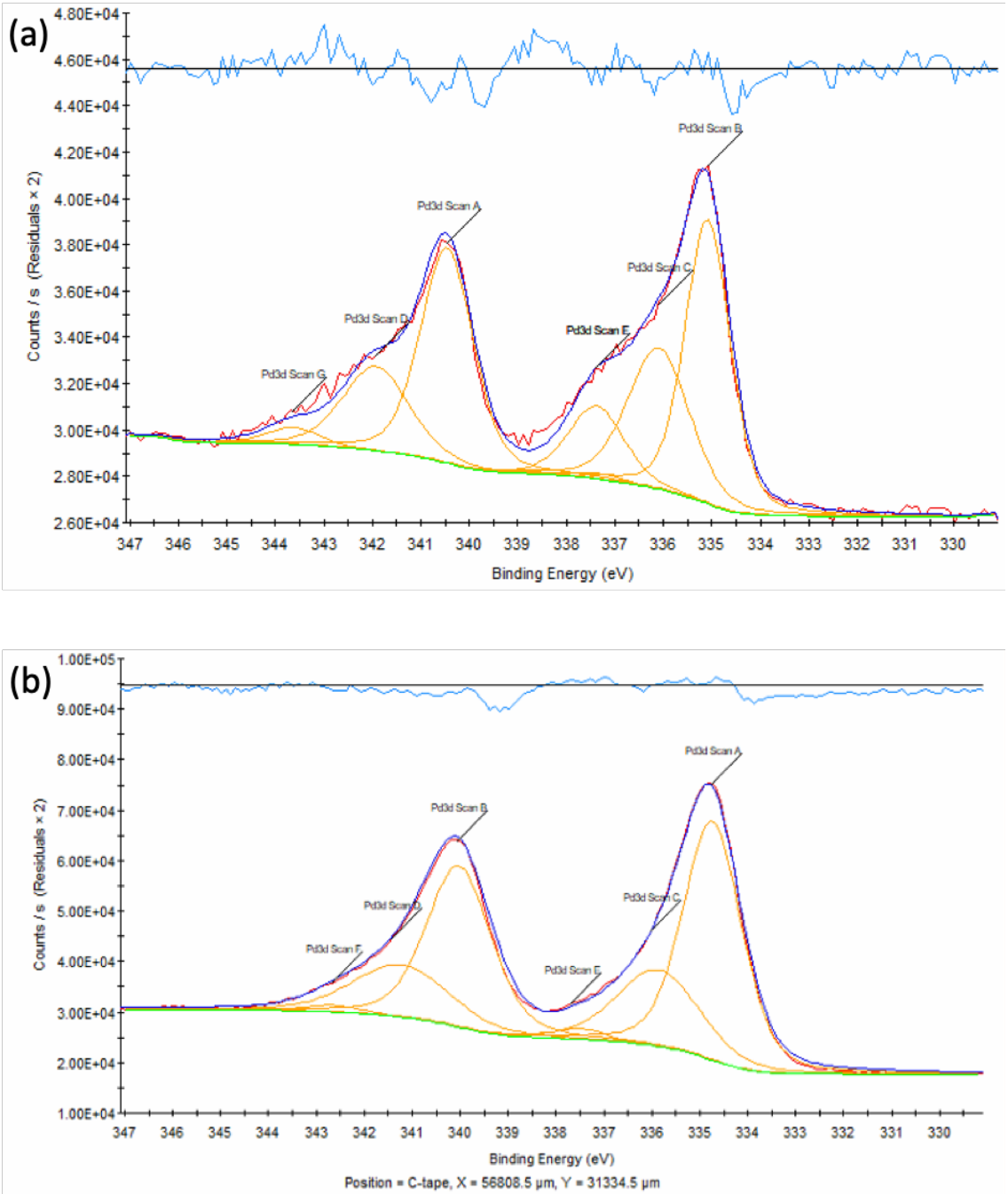

Figure S6. X-ray photoelectron (XPS) spectra for ligand-free Pd-CNT-SiO_2 (a) and commercial Pd on carbon (b) showing Pd 3d peaks. Orange curves correspond to peak fitting.

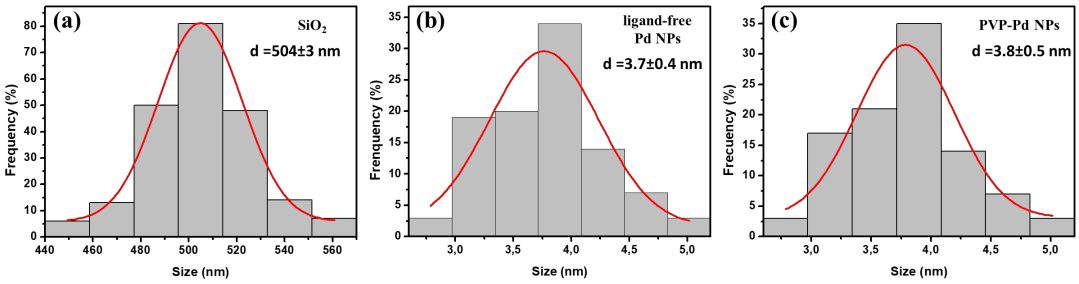

Figure S7. Histograms showing the particle size distributions of colloidal SiO_2 (a), ligand-free Pd NPs (b), and PVP-Pd NPs (c).

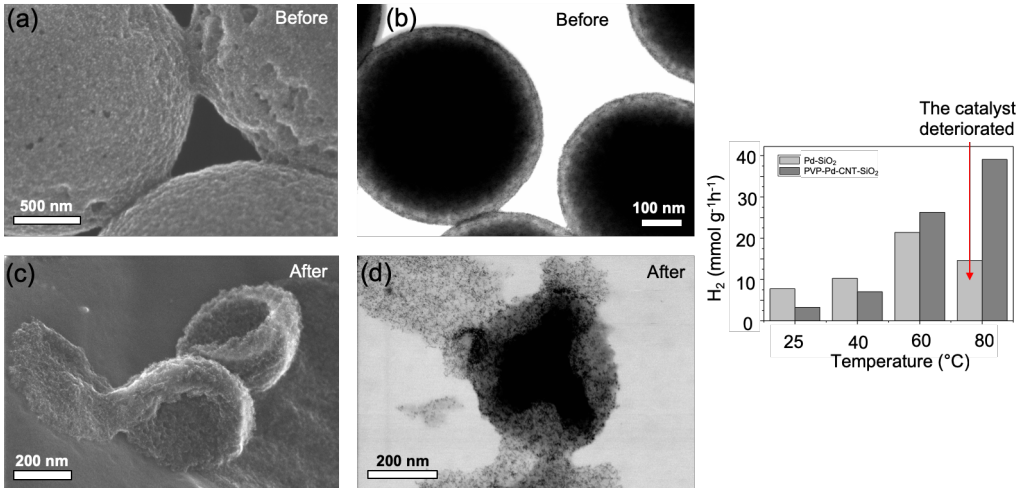

Figure S8. SEM (a,c) and TEM (b,d) images of Pd-SiO_2 before (a,b) and after (c,d) FA dehydrogenation reaction at 80°C. The bar graph on the right shows H_2 production rates as a function of temperature using ligand-free Pd-SiO_2 (light gray) and PVP-stabilized Pd-CNT-SiO_2 structures.

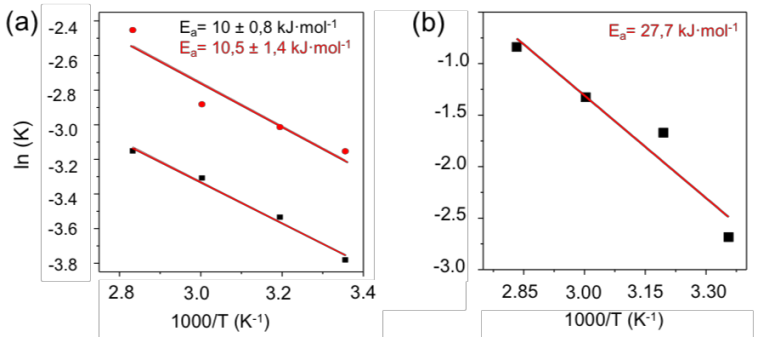

Figure S9. Representative Arrhenius plots for FA dehydrogenation reaction on Pd-CNT-SiO_2 structures (a: red and black points correspond to PVP-stabilized and ligand-free Pd, respectively) and commercial Pd on carbon (b).

Recyclability of ligand-free Pd-CNT-SiO_2 nanoparticles

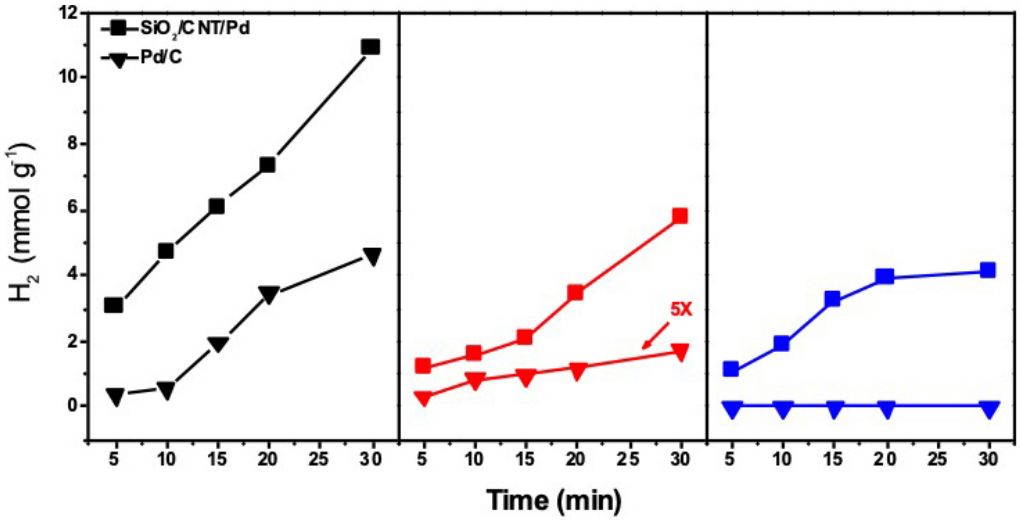

Figure S10. Recyclability tests of ligand-free Pd-CNT-SiO_2 and Pd/C structures showing the volume of H_2 production with elapsing time for three consecutive runs under otherwise same conditions. Prior to each repeated test using the same catalyst sample, the catalyst was rinsed with an excessive amount of ultrapure water, dried at 70°C, and dispersed in a fresh FA-SF solution at 80°C. Catalyst performance degradation might be associated with the loss and partial aggregation of the material during the purification step.

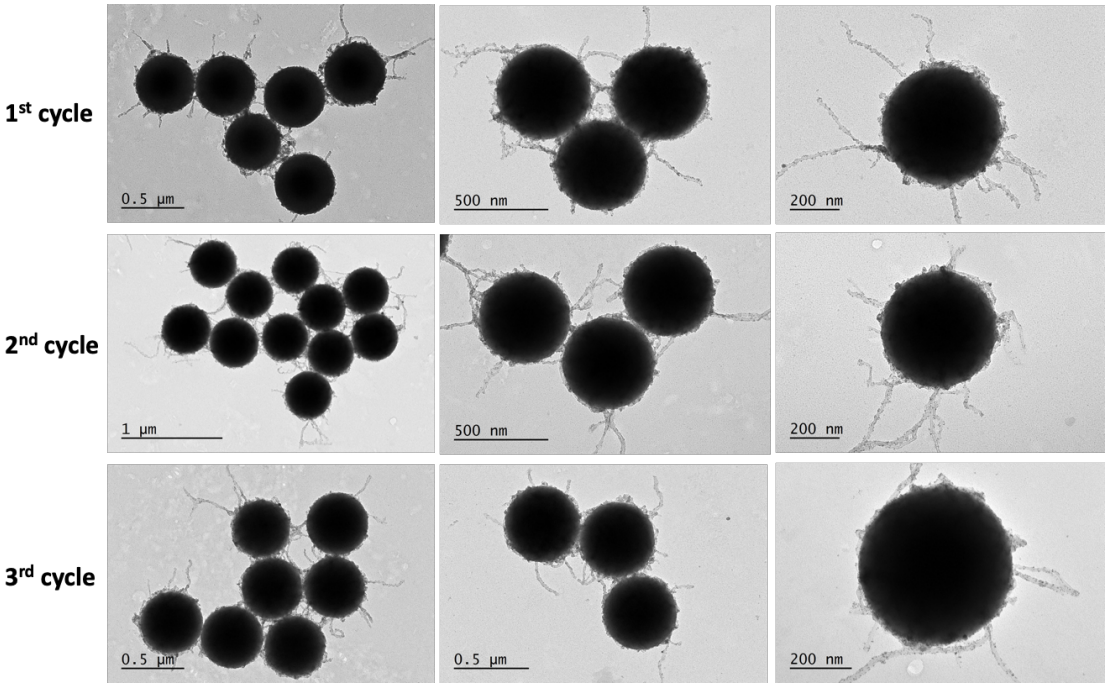

Figure S11. TEM images of ligand-free Pd-CNT-SiO_2 structures after each cycle of recyclability experiments shown in Figure S18.

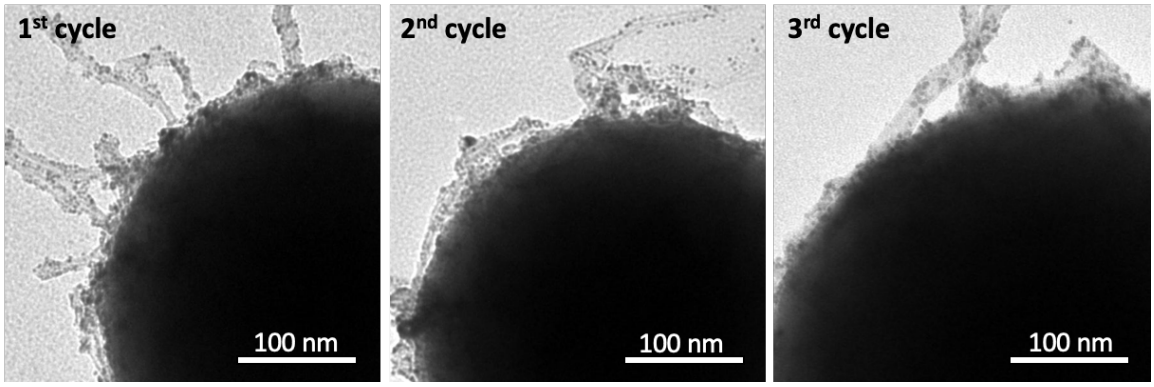

Figure S12. High magnification TEM images of ligand-free Pd-CNT-SiO_2 structures after each cycle of recyclability experiments shown in Figure S18.

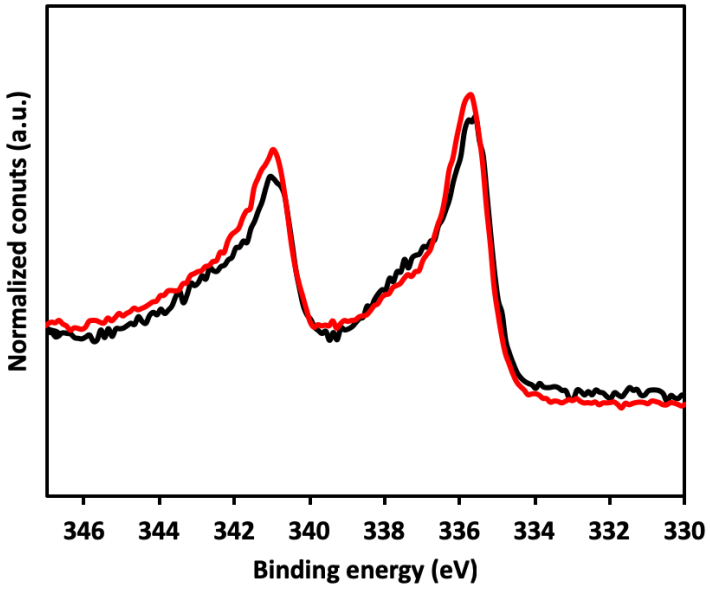

Figure S13. XPS spectra of ligand-free Pd-CNT-SiO_2 showing Pd 3d peaks before (black line) and after (red line) three cycles of FA-SF dehydrogenation at 80°C.

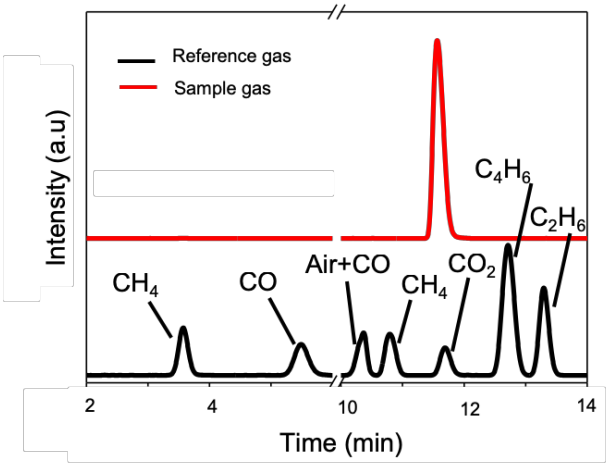

Figure S14. A representative gas chromatogram obtained using an FID equipped with a methanizer for the FA decomposition using Pd-CNT-SiO_2 catalyst (red trace) showing that no CO production was detected during the reaction. The amount of CO_2 matched the amount of H_2 detected with TCD and therefore corresponded to FA dehydrogenation pathway.

Theoretical calculations

All density functional theory (DFT) calculations were performed in the Vienna ab initio simulation package (VASP).[4,5] The exchange-correlation energy was treated by the spin-polarized generalized-gradient approximation (GGA) with the version of Perdew-Burke-Ernzerhof (PBE).[6] The projector augmented wave (PAW)[7] potential was used to describe the electron-ion interaction with a cutoff energy of 500 eV and fermi-level smearing of 0.1 eV. The 4x4x1 Monkhorst-Pack mesh was used for the k-point sampling of Brillounin zone on the slabs of Pd surfaces and Pd-CNT (carbon nanotube) surfaces. The slab sizes of Pd(111), Pd(110), Pd(100) and Pd(211) are $8.25\,Å \times 8.25\,Å$, $11.67\,Å \times 8.25\,Å$, $8.25\,Å \times 8.25\,Å$, $20.22\,Å \times 8.25\,Å$, respectively (see Fig. S11). For Pd-CNT systems, the slab sizes of $16.51\,Å \times 4.77\,Å$, $13.76\,Å \times 7.78\,Å$, $13.75\,Å \times 5.50\,Å$ and $13.48\,Å \times 5.50\,Å$ were used for Pd(111)-CNT, Pd(110)-CNT, Pd(100)-CNT and Pd(211)-CNT, respectively (see Fig. S12). To avoid the interaction between the slabs, 15 Å vacuum zone was modelled in the z direction of surface slabs. The electronic energy and force, 10^{-3}eV and 10^{-2} eV/Å per atom, were applied as the convergence criterion of geometry optimization.

As it is time-consuming to run calculation on Pd-CNT system with a large CNT, the CNT with the diameter of 5 Å was used in all the Pd-CNT systems. To test the rationality and accuracy of this model, we had carried out the calculation of the binding energy of adsorbed H* as the function of the diameter of CNT on Pd(111) surface. As shown in Fig. S17 and S18, it can be found that the binding energy of H* are almost not affected by the size of CNTs, which means that the effect of CNT size on the surface activity of Pd is negligible. Meanwhile, considering the experimental condition, the adsorption of hydroxyl on the CNT surface was considered in this paper.

The binding energy was applied to evaluate the binding strength of reaction intermediates, which was calculated as follows:

$$E_b = E_D + E_I - E_T$$

where E_I, E_I and E_T are the energies of an isolated surface slab, a gas-phase adsorbates and an adsorbed surface slab, respectively.

The Gibbs free energy was calculated as follows,

$$G = E + ZPE - TS$$

where E is the total electronic energy obtained directly from DFT calculations, ZPE is the zero-point energies (ZPE), T is the temperature which refers to room temperature (T=298.15K), and S is the entropy. The ZPE and entropies of free molecules were obtained from the standard thermodynamic database,[8] and those of adsorbed intermediates were calculated from the

vibrational frequencies. Since the electronic energies (E) of CO_2, H_2, HCOOH and adsorbed COOH* are overestimated by DFT, they were corrected by 0.45 eV, -0.009 eV, 0.2 eV and 0.2 eV, respectively.[9,10] Considering the estimation of the stabilization of hydrogen bond by species in aqueous solution, the Gibbs free energy of COOH* was correct by -0.25 eV.[10]

To understand the reaction pathways and mechanism, the Gibbs free-energy diagram was calculated based on the computational hydrogen electrode (CHE) model,[11] which defines that the chemical potential of a proton/electron (H^++e^-) in solution is equal to half of the

chemical potential of a gaseous H_2. The change of Gibbs free energies (ΔG)[11] was calculated as outlined below:

$$\Delta G = \Delta E + \Delta ZPE - T\Delta S + \Delta G_U$$

where ΔE, ΔZPE and ΔS are the change of electronic energy, zero-point energy and entropy, respectively, ΔG_U is the effect of the external potential to ΔG. For ΔG_U, it is shifted by –eU in each (H^++e^-) transfer step, where e is the number of electrons transferred and U is the applied bias.

Here three main reaction pathways were considered according to the previous research,[12,13] as shown in the Fig. 3a (main text). Three different reaction pathways were considered for the decomposition of formic acid: Path I (formate pathway) and Path II (carboxyl pathway), which are dehydrogenation with the products of CO_2 and H_2, and Path III, which is dehydration with the products of CO and H_2O.

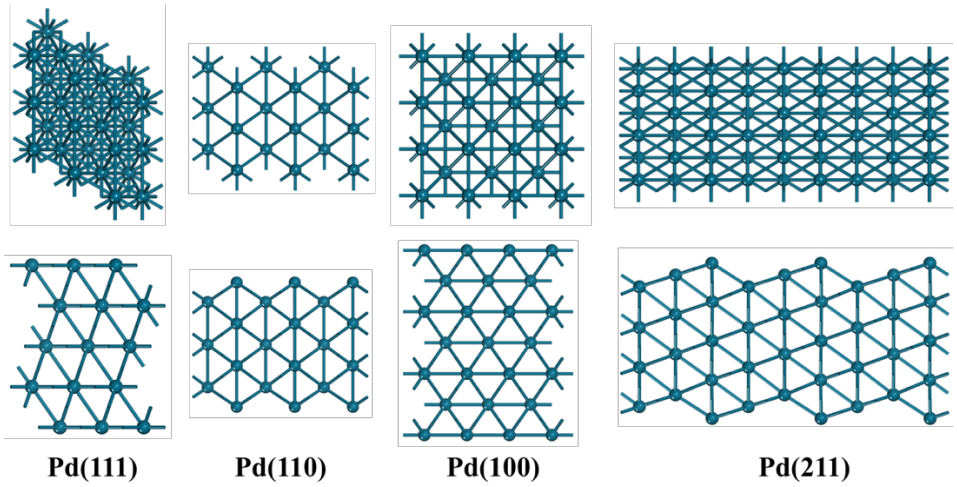

Figure S15. Top and side views of optimized model slabs for Pd(111), Pd(110), Pd(100) and Pd(211).

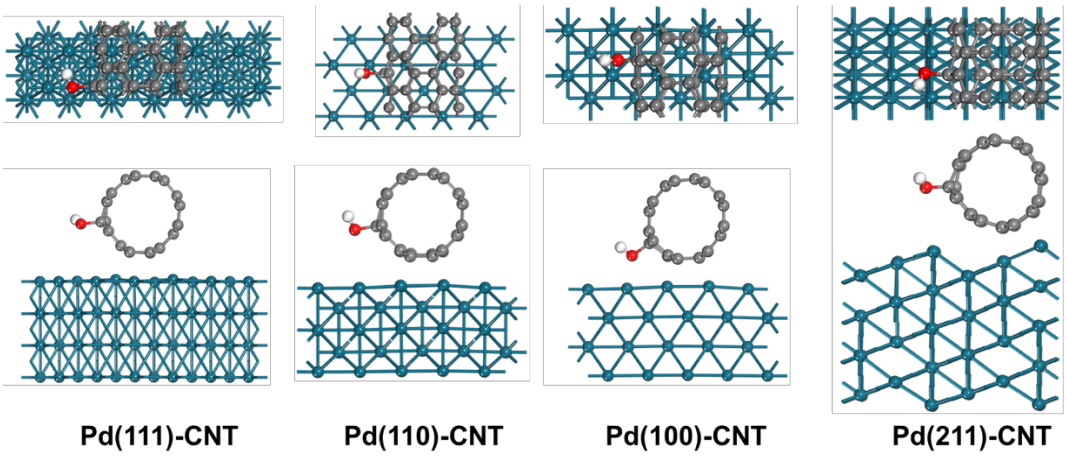

Figure S16. Top and side views of optimized model slabs for Pd(111)-CNT, Pd(110)-CNT, Pd(100)-CNT and Pd(211)-CNT. The adsorption of hydroxyl is considered.

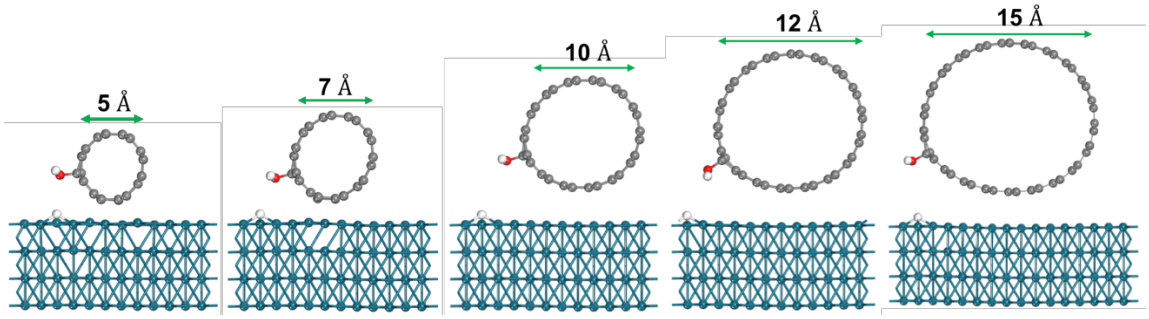

Figure S17. Optimized adsorption structures of H* on Pd(111)-CNT with carbon nanotubes of different sizes.

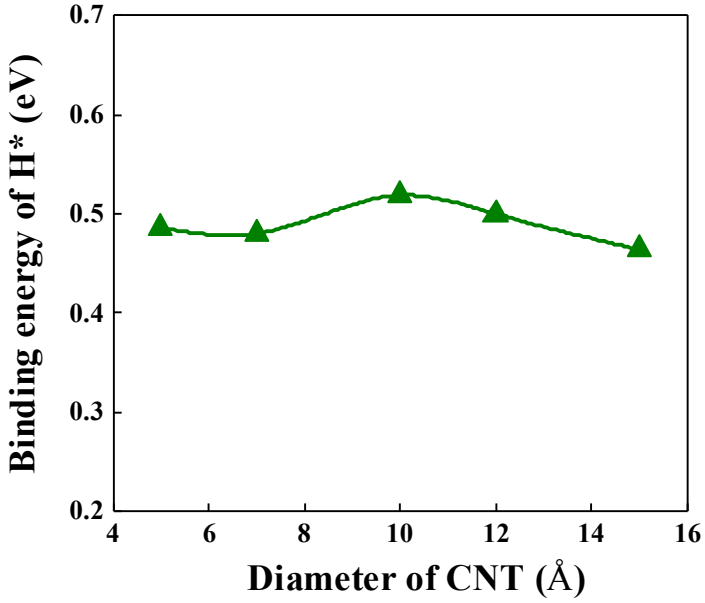

Figure S18. The effect of CNT's diameter of Pd(111)-CNT on the binding energy of adsorbed H*.

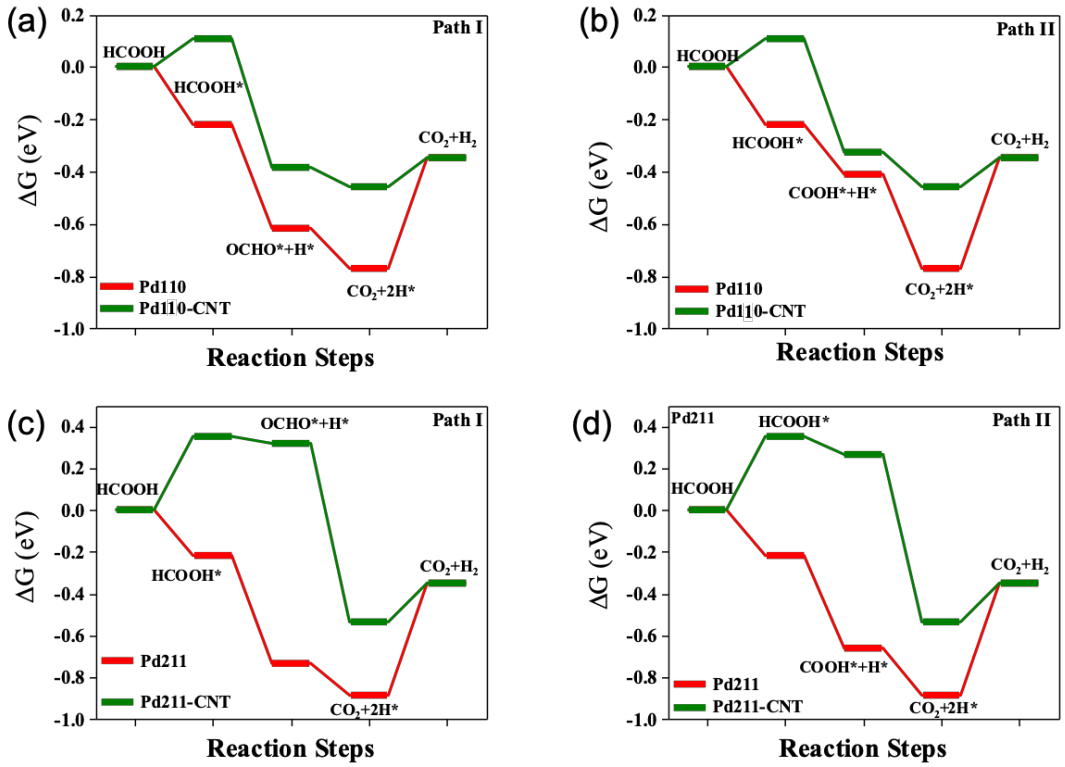

Figure S19. Free energy diagrams for FA dehydrogenation paths I (a,c) and II (b,d) (according to Fig. 3a, main text) on pristine (red lines) and interfaced with CNT (green lines) Pd(110) (a,b) and Pd(211) (c,d) surfaces.

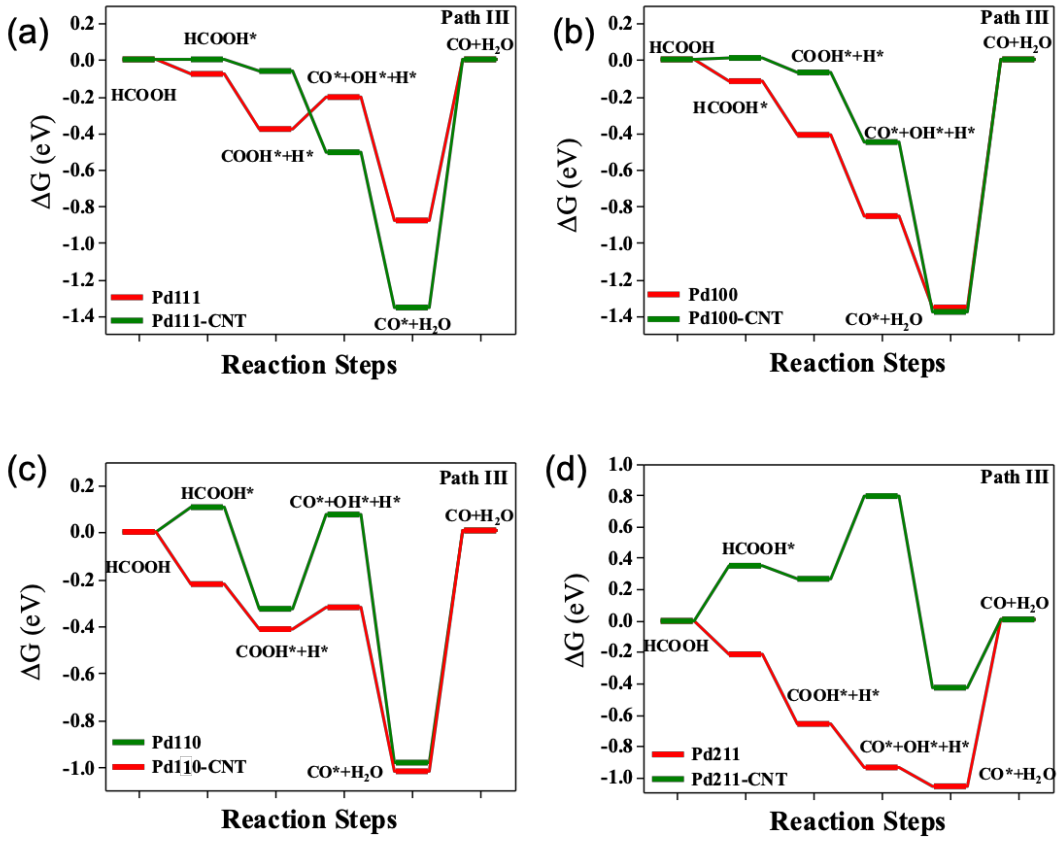

Figure S20. Free energy diagrams for FA dehydration, path III (Fig. 3a, main text) on pristine and interfaced with CNT Pd(111) (a), Pd(100) (b), Pd (110) (c) and Pd(211) (d) surfaces.

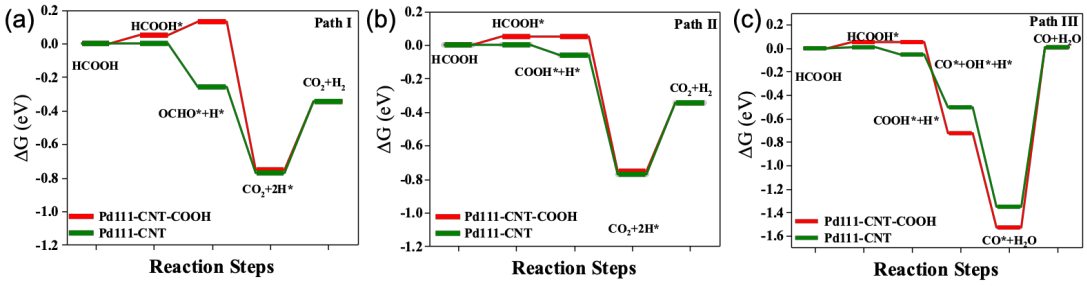

Figure S21. *COOH and *OH have a similar effect on the catalytic activity of Pd-CNT complex for HCOOH dehydrogenation since they don't change the rate-limiting steps and the corresponding energy barriers.

Table S1: gas phase molecules and their thermodynamic quantities, including DFT total electronic energy(E), zero-point energy (ZPE), entropy multiplied by temperature (TS) and Gibbs free energy.

Molecule	*E*(eV)	*ZPE*(eV)	*TS*(eV)	*G*(eV)
CO	-14.78	0.13	0.61	-15.26
CO_2	-22.95	0.31	0.66	-23.30
H_2	-6.77	0.27	0.40	-6.90
H_2O	-14.21	0.56	0.58	-14.23
HCOOH	-29.87	0.89	0.72	-29.70

Table S2: adsorbate molecules and their thermodynamic quantities on Pd surfaces, including DFT total electronic energy(E), zero-point energy (ZPE), entropy multiplied by temperature (TS) and Gibbs free energy.

	E(eV)	*ZPE*(eV)	*TS*(eV)	*G*(eV)
Pd111				
HCOOH*	-350.557	0.890	0.170	-349.837
OCHO*+H*	-350.720	0.797	0.150	-350.073
COOH*+H*	-350.721	0.792	0.164	-350.093
2H*	-328.254	0.364	0.012	-327.902
CO*+HO*+H*	-350.490	0.721	0.200	-349.969
CO*	-336.483	0.194	0.115	-336.404
Pd110				
HCOOH*	-340.995	0.902	0.171	-340.264
OCHO*+H*	-341.281	0.787	0.168	-340.662
COOH*+H*	-341.062	0.783	0.175	-340.454
2H*	-318.257	0.338	0.048	-317.967
CO*+HO*+H*	-340.818	0.693	0.239	-340.364
CO*	-326.906	0.194	0.113	-326.825
Pd100				
HCOOH*	-347.179	0.897	0.176	-346.458
OCHO*+H*	-347.305	0.774	0.173	-346.704
COOH*+H*	-347.294	0.775	0.177	-346.696
2H*	-324.481	0.322	0.052	-324.211
CO*+HO*+H*	-347.712	0.7189	0.201	-347.1941
CO*	-333.565	0.2019	0.101	-333.4641
Pd211				
HCOOH*	-611.078	0.894	0.174	-610.358
OCHO*+H*	-611.492	0.788	0.165	-610.869
COOH*+H*	-611.362	0.784	0.174	-610.752
2H*	-588.463	0.338	0.046	-588.171
CO*+HO*+H*	-611.589	0.72	0.213	-611.082
CO*	-597.039	0.193	0.116	-596.962

Table S3: adsorbate molecules and their thermodynamic quantities on Pd-CNT surfaces, including DFT total electronic energy(E), zero-point energy (ZPE), entropy multiplied by temperature (TS) and Gibbs free energy.

	E(eV)	*ZPE*(eV)	*TS*(eV)	*G*(eV)
Pd111-CNT				
HCOOH*	-563.652	0.899	0.169	-562.922
OCHO*+H*	-563.817	0.786	0.153	-563.184
COOH*+H*	-563.563	0.779	0.166	-562.950
2H*	-541.168	0.338	0.016	-540.846
CO*+HO*+H*	-563.878	0.708	0.258	-563.428
CO*	-550.134	0.192	0.100	-550.042
Pd110-CNT				
HCOOH*	-710.613	0.902	0.171	-709.882
OCHO*+H*	-710.992	0.787	0.168	-710.373
COOH*+H*	-710.872	0.783	0.175	-710.264
2H*	-687.888	0.338	0.048	-687.598
CO*+HO*+H*	-710.370	0.693	0.239	-709.916
CO*	-696.816	0.194	0.113	-696.735
Pd100-CNT				
HCOOH*	-517.175	0.897	0.176	-516.454
OCHO*+H*	-517.189	0.774	0.173	-516.588
COOH*+H*	-517.487	0.775	0.177	-516.889
2H*	-494.485	0.322	0.052	-494.215
CO*+HO*+H*	-517.433	0.719	0.201	-516.915
CO*	-503.710	0.202	0.101	-503.609
Pd211-CNT				
HCOOH*	-580.311	0.894	0.174	-579.591
OCHO*+H*	-580.248	0.788	0.165	-579.625
COOH*+H*	-580.237	0.784	0.174	-579.627
2H*	-557.622	0.338	0.046	-557.330
CO*+HO*+H*	-579.659	0.720	0.213	-579.152
CO*	-566.214	0.193	0.116	-566.137

References:

[1] Q. He, X. Cui, F. Cui, L. Guo, J Shi, *Microporous Mesoporous Mater.*, 2009, **117**, 609–616.

[2] M. Sanles-sobrido, M. A. Correa-duarte, L. M. Liz-marzan, *Small*, 2008, **4**, 583–586.

[3] B. B. Lim, M. Jiang, J. Tao, P. H. C. Camargo, Y. Zhu, Y. Xia, *Adv. Funct. Mater*. 2009, **19**, 189–200.

[4] P. E. Blöchl, *Phys. Rev. B: Condens. Matter Mater. Phys.*, 1994, **50**, 17953−17979.

[5] G. Kresse, J. Furthmüller, *Phys. Rev. B: Condens. Matter Mater. Phys.*, 1996, **54**, 11169−11186.

[6] M. C. Payne, M. P. Teter, D. C. Allan, T. A. Arias, J. D. Joannopoulos, *Rev. Mod. Phys.*, 1992, **64**, 1045−1097.

[7] G. Kresse, D. Joubert, *Phys. Rev. B: Condens. Matter Mater. Phys.*, 1999, **59**, 1758−1775.

[8] C. J. Cramer, *Essentials of Computational Chemistry Theories and Models*, 2nd ed., 2004, John Wiley & Sons: West Sussex, England.

[9] J. S. Yoo, R. Christensen, T. Vegge, J. K. Nørskov, F. Studt, *ChemSusChem*, 2016, **9**, 358.

[10] R. Christensen, H. A. Hansen, T. Vegge, *Catal. Sci. Technol.*, 2015, **5**, 4946.

[11] J. K. Norskov, J. Rossmeisl, A. Logadottir, L. Lindqvist, J. R. Kitchin, T. Bligaard, H. J. Jonsson, *J. Phys. Chem. B*, 2004, **108**, 17886−17892.

[12] J. A. Herron, J. Scaranto, P. Ferrin, S. Li, M. Mavrikakis, *ACS Catal.*, 2014, **4**, 4434−4445.

[13] J. S. Yoo, F. A. Pedersen, J. K. Nørskov, F. Studt, *ACS Catal.*, 2014, **4**, 1226−1233.